RSC Advances

ROYAL SOCIETY OF CHEMISTRY

www.rsc.org/advances

Utilization of a pyrrole derivative based antimicrobial functionality impregnated onto $CaO/g\text{-}C_3N_4$ for dyes adsorption

Sherif A. Younis[a, b*]; Ahmed Abd-Elaziz[c]; Ahmed I. Hashem[c]

[a] Analysis and Evaluation Department, Egyptian Petroleum Research Institute, 11727 Nasr City, Cairo, Egypt.

[b] Central Laboratories, Egyptian Petroleum Research Institute, 11727 Nasr City, Cairo, Egypt.

[c] Chemistry Department, Faculty of Science, Ain Shams University, 11566 Abassia, Cairo, Egypt.

*Correspondence: Sherif A. Younis

E-mail: sherifali@epri.sci.eg; sherifali_r@yahoo.com

Tel.: (+201) 228877458; **Fax:** (+202) 22747433.

Abstract

A novel functionalization of CaO/g-C_3N_4 based nanocomposite using 4,5-diphenyl-2-thioxo-2,5-dihydro-1H-pyrrole-3-cabonitrile (P3C@CaO-HCN) was performed for wastewater remediation from organic dyes and microbial pollutants. Adsorption performance of multiple mixtures of basic and acidic dyes by P3C@CaO-HCN was investigated and optimized using three-level Box–Behnken design of experiment (BBD-DOE). The quadratic Box-Behnken polynomial equation showed best fitted with the experimental adsorption capacities of crystal violet (CV), methylene blue (MB), and methyl orange (MO) model dyes. The simultaneous influence of adsorption conditions was tested based on the developed Box-Behnken equation, 3D contour plots, and ANOVA analysis. Nonlinear regression analysis of kinetics and isotherm constants were computed and validated to propose the adsorption mechanism. Adsorption is found within the ranges of endothermic physical adsorption (ΔH°= 6.17 to 8.58 KJ/mol) and controlled by both π-π and electrostatic forces depending on the pH level beside film diffusion mechanism. The maximum adsorption affinity can arrange in the order of MB > CV ≥ MO with q_e (μmol/g) of 1915.8, 1227.8, and 1221 μmol/g, respectively. At 500 mg/l P3C@CaO-HCN as minimum inhibitory dose, the inhibition rate (I%) were 87.9%, 46.9%, and 72.5% for *E. coli*, *P. aeruginosa*, and *C. albicans*, respectively. The antimicrobial effect can result from the free cyanide (C≡N) functionality of a pyrrole-3-cabonitrile and protonated g-C_3N_4 (HCN) sheet, which depend on the P3C@CaO-HCN concentration and pathogen types.

Keywords: 4,5-diphenyl-2-thioxo-2,5-dihydro-1H-pyrrole-3-cabonitrile; protonated carbon nitride; CaO nanoparticle; adsorption; antimicrobial activity; Box–Behnken design of experiment (BBD-DOE).

1. Introduction

Many kinds of water pollutions have already become existed, including organics, inorganic, microorganism, and so on. Dyes contaminated water environments have been generated ever since the dyestuffs were fabricated and recently become one of the largest water defilers in the world. At present, over one hundred thousand of the dyestuffs are daily consumed in industry to color various kinds of materials [1–3]. Crystal violet (CV) and methylene blue (MB), basic dyes, are used a lot for coloring paper, dyeing cotton, and wools [2,4,5]. Methyl orange (MO), an acidic dye containing the azo group (N═N), is quite used in the printing, food, pharmaceutical, paper, and textile industries [2,6]. Both basic and acidic dyes have significant concerns because of their toxicity to aquatic creatures and human beings [6,7]. But, the basic dyes are more toxic than the acidic dyes, because of their easily interact with negative cell membrane, and/or entrance into living cells and concentrate in the cytoplasm to cause mitotic poison [4,7].

Adsorption is shown the most effective technique for dye removal because of its easy operation and the ability to treat concentrated dyestuffs with the possibility of regeneration [1,2,4,7–10]. Most of the developed adsorbents in the literature do not have an effective treatment performance for the effluents have multi-dyes (basic and acidic) constituents as industrial cases. More recently, regarding increasing types of water pollutions, the exploitation of multifunctional materials has received enormous attention in research communities. To date, there are a few literature on the preparation of multifunctional materials for dye adsorption and microbial purification. For example, Jiang et al. (2016) studied the application of magnetic chitosan–graphene oxide (MCGO) composite as adsorbent for MO dye (398.08 mg/g) and antibacterial towards *Escherichia coli*. Al-Sagheer et al. (2014) investigated the uptake of different dyes (EBT, MV, and MB) and cytotoxicity against different bacteria and fungi using chitosan-g-poly (N-acryloyl morpholine) copolymer and they noted that the copolymer exhibits greater affinities of acid dye adsorption and antibiological activity towards *E. coli*. However, to the best of our survey, there is no literature to explore the antimicrobial and dye adsorption performance of 4, 5-diphenyl-2-thioxo-2, 5-dihydro-1H-pyrrole-3-cabonitrile, and protonated carbon nitride (HCN).

In view of the above facts, the aim of this work is to fabricate a new multifunctional material for the effective wastewater remediation from multi-dyes (CV, MB, and MO) pollutants with simultaneous antimicrobial properties. As a result, P3C@CaO-HCN multifunctional nanomaterial prepared by the reaction of 4, 5-diphenyl-2-thioxo-2, 5-dihydro-1H-pyrrole-3-cabonitrile hetero-aromatic with CaO nanoparticles impregnated onto protonated carbon nitride sheet (HCN) was obtained and characterized. Four variables, three-level Box-Behnken design of experiment (BBD-DOE) was applied to investigate the linear and nonlinear influence of the

adsorption variables and provides a mathematic equation for optimization of dye adsorption. Kinetic, isotherm, and thermodynamic theories were investigated and statistically validated to understand the rate-controlling steps involved in the adsorption process. The antimicrobial activity of the P3C@CaO-HCN nanocomposite was further tested against three selected microorganisms, including *Escherichia coli*, *Pseudomonas aeruginosa* and *Candida albicans* strains, as widely distribution pathogens in water environments.

2. Experimental

2.1. Synthesis of 4, 5-diphenyl-2-thioxo-2, 5-dihydro-1H-pyrrole-3-cabonitrile (P3C)

A mixture of 10 mmol 4, 5-diphenyl-2-oxo-2, 5-dihydro-1H-pyrrole-3-cabonitrile [12] and 20 mmol P_2S_5 in 30 ml dry toluene was refluxed for 8h. After that, the solvent was decanted under reduced pressure and the solid obtained was filtered off, washed and then recrystallized from benzene in dark red needles. The obtained reddish crystals of 4, 5-diphenyl-2-thioxo-2, 5-dihydro-1H-pyrrole-3-cabonitrile (yield 60% and m.p 476- 478 K) was labeled as P3C. The characteristics structure of the obtained P3C (thioxo pyrrole derivative) were presented as follow. FTIR (KBr) cm^{-1}: 3350 (NH), 1250 (C=S), 2360 (C≡N). ^{1}H-NMR (DMSO-d_6): δH (ppm) 2.51 (br.s, 1H, NH, exchangeable with D_2O), 4.63 (s, 1H, -CHPh), 7.02-7.77 (m, 10H, ArH). MS, m/z (%): 278 (M^+, 72), 260 (45), 248 (15), 231 (17), 105 (30), 74 (90), 59 (100). Anal. Calcd. For C17H12N2S (276.36): C, 73.88; H, 4.38; N, 10.14; S, 11.60. Found: C, 74.01; H, 4.47; N, 9.98; S, 11.82.

2.2. Synthesis of g-C_3N_4 and CaO nanomaterials

The g-C_3N_4 was prepared by microwave thermal condensation of 20 g urea (99%, Aldrich) in a covered alumina crucible for 1h at 700 watts. The resulting yellow product was then HCl-treated in a quartz reactor containing 1 mol HCl at 348 K under vigorous stirring for 12 h. The protonated product was collected, washed with hot deionized water, and then vacuum dried at 373K and coded as protonated carbon nitride (HCN).

Calcium oxide nanoparticles were prepared from eggshells substrate. Typically, the free membrane eggshells were grounded and then purified by dichloromethane in an ultrasonic bath for 2 h at 333 K then filtered and dried at 393K. The powder was then calcined in a microwave oven at 700 watts for 90 minutes and the obtained white powder was coded as CaO nanoparticles.

2.3. Fabrication of P3C@CaO-HCN nanocomposite adsorbent

The P3C@CaO-HCN nanocomposite was prepared according to the procedure described hereinafter, which was also depicted in Scheme (1). In the first step, a mixture of CaO and HCN (1:3) were completely dispersed in 100 ml ethanol/water solutions placed in 60 Hz ultrasonic bath for 1 h, then aged overnight at 363K under stirring. The CaO-HCN nanocomposite obtained was

then collected by centrifugation and calcined at 553K for 2h. In the next step, the CaO-HCN sample was dispersed in 50 mL ethanol/acetic acid anhydrous (1:0.2) solutions and sonicated for 30 minutes. To this dispersion, 15 ml ethanol solution of P3C heteroaromatic functionalities was added over 3h, after that, aging for another 36 h at 363 K and stirring speed of 700 rpm. After the reaction stopped, the obtained powder of P3C@CaO-HCN nanocomposite, with nominal ratios of 1: 3: 0.5 was collected, washed, and vacuum dried at 363 K.

2.4. Analytical procedures

Melting points were measured on a Gallen Kamp electric melting point apparatus. The ^{1}H-NMR spectra were run at 300 MHz on a GEMINI 300 BB NMR spectrometer using tetramethylsilane (TMS) in DMSO-d_6 as the internal standard. The mass spectra were recorded on a Shimadzu GC-MS QP-1000EX mass spectrometer operating at 70 eV. FTIR spectra were obtained using KBr disc on a spectrum one Perkin Elmer FT-IR spectrophotometer. The phase structural was determined by X-ray powder diffraction (XRD, Xpert PRO, PAN analytical, Netherlands) at 1.54056˚A Cu Kα radiation and a D8 Bruker diffractometer (40 kV and 30 mA). A high-resolution transmission electron microscopy (HR-TEM) images were recorded on a JEOL JEM-2, 100 electron microscope at 200 kV accelerating voltage.

2.5. Batch adsorption tests

A stock water solutions of 2000 µmol/l of CV, MB, and MO multi-dyes was first prepared in synthetic wastewater containing 1055 mg/L inorganic dissolved solids similar to the characteristic of previously collected dyestuff industrial wastewater in Egypt (data not shown). All batch adsorption runs were conducted in a 125 mL closed shaking flasks at 150 rpm fixed shaking speed.

2.5.1. Box-Behnken design of experiment (BBD-DOE)

The optimum variables for optimizing P3C@CaO-HCN adsorbent for the adsorption of CV, MB, and MO multi-dyes were set by a rotatable, four-variables, three-level Box–Behnken design (BBD). The three-level independent variables were set as solution pH (X_{pH}=3, 6, 9), composite dose (X_D= 0.5, 1.0, 1.5 g/l), initial dyes concentrations (X_{Co}=200, 600, 1000 µmol/l), and solution temperature (X_T =288, 308, 328 K). The levels of independent variables were selected based on our assessment of Al-Gharbia textile industries in Egypt (data not shown). The adsorption capacities (q_e, µmol/g) of CV (Y_{CV}), MB (Y_{MB})and MO (Y_{MO})dyes by P3C@CaO-HCN were selected as response factors. Based on BBD-DOE design matrix, a total 29 batch experimental runs (runs= 2^4+2*4 + 5 controlled points) were studied. The 29 BBD-DOE responses results obtained were then analyzed using the MINITAB (v. 17) and Design-Expert (v.

7.0.1) software to develop a numerical regression equation to express the relation between the dyes responses and the independent variables under tested conditions.

2.5.2. Adsorption studies

For statistical BBD-DOE adsorption design, 29 series of lab flasks with the desired level of the variables combination were placed on an orbital shaker and agitated for 24 h. At the optimum BBD-DOE conditions: kinetic, thermodynamic and isotherm studies were conducted. The kinetic and thermodynamic studies were carried out at $X_{Co} = 1000$ µmol/l initial dyes concentrations with varying temperatures (288 K to 328 K) for ten intervals time up to 24 h. The isotherm test was performed using 10 series of initial dyes concentrations ranging from 50 to 1600 µmol/l. The other adsorption conditions were set on the basis of the optimum BBD-DOE results obtained. After adsorption processes, the residual dyes concentrations were determined by a double beam UV-visible spectrophotometer in the clear water solutions after centrifugation. Dyes concentrations in the treated wastewater were calculated from the corresponding linear calibration curves for each dye at their λ_{max} values of 586 nm, 668 nm, and 464 nm for CV, MB, and MO, respectively. The dyes removal percentage (Y%) and adsorption capacities (µmol/g) were calculated using the following equations (Eqs. 1 -2):

$$Y\% = \frac{(C_o \leftarrow C_t)}{C_o} x100 \text{ (Eq. 1)}$$

$$q_t = \frac{C_o \leftarrow C_t}{m} V \text{ (Eq. 2)}$$

Where C_o and C_t (µmol/l) are the dyes concentrations at initial and t time, respectively, V (L) is the water volume and m (g) is the adsorbent dose.

2.6. Statistical models validation and error analysis

The adequacy of the simulated models and their validation were assessed using different descriptive statics including a non-parametric Mann–Whitney U-test and a parametric two-sample (unpaired) t-test in accordance with the analysis of variance (ANOVA) at a probability level of 0.05 [4]. Error statics; including the root mean square error of prediction (RMSEP), the relative standard error of prediction (RSEP), chi-square (X^2) tests, and the average relative error (ARE%) were also calculated to reflect the suitability of the simulated mathematical models to predict the adsorption responses [4,13,14]. The statistical validation and error studies were checked by using the solver add-in with Microsoft Excel@2013, MINITAB (v.17) and IBM-SPSS (v. 21) statistical package for the verification of the results obtained.

$$RMSEP = \sqrt{\frac{\sum_{i=1}^{N}(Y_{pred,i} - Y_{exp,i})^2}{N}} \text{ (Eq. 3)}$$

$$RSEP = \sqrt{\frac{\sum_{i=1}^{N}(Y_{pred,i}-Y_{exp,i})^2}{\sum_{i=1}^{N}(Y_{exp,i})^2}} \times 100 \text{ (Eq. 4)}$$

$$X^2 = \sum_{i=1}^{N}\left|\frac{(Y_{exp,i}-Y_{pred,i}}{Y_{exp,i}}\right|^2 \text{ (Eq. 5)}$$

$$ARE\% = \frac{100}{N}\sum_{i=1}^{N}\left(\frac{(Y_{exp,i}-Y_{pred,i}}{Y_{exp,i}}\right) \text{ (Eq. 6)}$$

Where $Y_{pred,i}$and $Y_{exp,i}$ are the model predicted and experimental response values and N is the number of experimental runs.

3. Results and discussion

Pyrrole is an important heterocycle because its structure is incorporated into many natural products e.g., heme, chlorophyll, vitamin B12, and the bile pigment. Also, the pyrrole ring is present in various drugs, including immunosuppressant, analgesic, anti-tubercular agents, and COX-2 inhibitors. In our earlier investigation[12], 4,5-diphenyl-2-oxo-2,5-dihydro-1H-pyrrole-3-cabonitrile preparation was reported by our research group. In the present work, we have modified the pyrrolone derivatives into its thioxo derivative through converting the oxocarbonyl group (C=O) at position-2 into the thiocarbonyl group (C=S) by reaction with P_2S_5 in dry toluene (Scheme 1) (cf. experimental part). The thiocarbonyl group, which is known to be more electron rich and polarizable than C=O group, existing as a thione/thiol tautomers with the N-H group in the 1H-pyrrole derivative. The presence of the two active functionalities of thiol (–SH) and cyanide (–CN) obtained in the 4, 5-diphenyl-2-thioxo-2, 5-dihydro-1H-pyrrole-3-cabonitrile (P3C) promoted our interest to construct an active functional component onto CaO-HCN nanocomposite through thiol group. This resulting in the formation of a strong S-O bond on the CaO-HCN nanocomposite surface and free cyanide (–C≡N) group as confirmed by the FTIR (cf. 3.1 part). The developed P3C@CaO-HCN showed multifunctional application for the adsorption of CV, MB, and MO organic dyes and wastewater purification from microbial pathogens because of the free cyanide group as described hereinafter and depicted in Scheme (1).

3.1. Structure characterization of the P3C@CaO-HCN

XRD spectra are used to test the phase structures and purity of the samples. The set of XRD diffraction peaks (Fig. 1a) shows the pure crystal phases of CaO NPs (2Θ=18.10 °, 32.3, 37.4 °, 53.90 °, 64.20 °, and 67.40°) and g-C_3N_4 (HCN) (2Θ=13° and 27.4°) with no more other impurities peaks. For CaO-HCN hybrid nanocomposite, the XRD patterns assigned for both CaO NPs and g-C_3N_4 were beside a minor amount of $Ca(OH)_2$ phase resulted during CaO impregnation in the water atmosphere. The HCN peak at 27.4° (0 0 2) become weaker, which was the result from restraining the stacking of HCN perpendicular to the 0 0 2 directions, the graphtic

stacking of the conjugated aromatic system, owing to introducing CaO NPs [15]. These results imply that CaO NPs deposit on the surface of HCN sheet and not incorporate into the HCN lattice [15,16]. Also, The XRD data showed that microwave thermal method is sufficient to achieve complete thermal decomposition of carbonate in eggshells to pure CaO phase and thermal condensation of urea to graphtic carbon nitride (g-C_3N_4). The determined crystallite size of the prepared CaO/g-C_3N_4 sample using the Scherrer formula [17] at $2\Theta = 37.4^o$ computed as 65.6 nm compared to CaO NPs crystal size of 58.42 nm.

The FTIR of functional P3C@CaO-HCN nanocomposite (Fig. 1b) showed similar characteristic features to their starting components with a slight red shift to a higher wavenumber compared to HCN, CaO NPs, and P3C materials. A band ranging from 3000-3600 cm^{-1} is originated from the vibration modes of the free N-H (pyrrole group) and the O-H of adsorbed H_2O by CaO NPs. The sharp breathing vibration band at ca. 810 cm^{-1} is assigned to the g-C_3N_4 tri-s-triazine units [18]. Absorption bands in the region between 1200–1700 cm^{-1} are corresponding to the skeletal C–N heterocycles stretches, comprising trigonal (N–$(C)_3$) and bridging C–NH–C units of the extended C-N-C network at g-C_3N_4 [18]. In contrary, the decreased of the intensive bands at ca. 3600 cm^{-1} (O-H) and ca. 500 cm^{-1} (Ca-O vibration) in P3C@CaO-HCN compared to starting components is a sign for P3C formation complexation on the CaO NPs surface rather than HCN. The disappear of C=S thiocarbonyl stretch band at ca. 1250 cm^{-1} (P3C) and appear of the band at ca.760 cm^{-1} and 1015 cm^{-1} ascribed to S-O stretching bonds (P3C@CaO-HCN) between P3C functionalities and Ca-O through thiol groups. Observation results suggest that the strengthening interaction bonds in the resultant P3C@CaO-HCN nanocomposite sample during self-assembly preparation approach.

The P3C@CaO-HCN morphological structure was examined using HRTEM image shown in Fig. 2a. HRTEM image showed spherical CaO NPs incorporated with both de-agglomerated and agglomerated distribution on the smooth surface of HCN with an average diameter of 60.7 nm. Also, HCN displayed a platelet-like morphology and a two-dimensional sheet structure. The pH zero point charge (pH_{ZPC}) of HCN, CaO NPs, and P3C@CaO-HCN samples were determined by both potentiometric mass titration and salt addition methods after 24 h of equilibration [19]. The resultant pH values using a pH meter model Mettler Toledo (Seven Go, IP67) are plotted in Fig. 2b. A significant change in the pH_{ZPC} surface charge properties was observed, which is calculated as 5.09, 10.52, and 5.82 for HCN, CaO NPs, and P3C@CaO-HCN, respectively.

3.2. Statistical modeling and optimization of the adsorption variables by RSM method

3.2.1. Statistical model simulation

The three-level BBD-DOE approach was adopted for studying the linear and simultaneous effects of the four adsorption variables to enhance the adsorption properties of P3C@CaO-HCN. Based on BBD-DOE experiments, the obtained minimum and maximum responses were found to be between 110.8-1013.9 µmol/g, 116.5-1455.8 µmol/g, and 69.7-1007.9 µmol/g for MB, and MO dyes, respectively. The BBD coupled with DOE analysis suggests the nonlinear polynomial regression model (Eq. 8) as the best-fitted expression between the dyes responses and the coded variables (X_{pH}, X_D, X_{Co}, X_T) with β as the regression coefficient term.

$$Y = \beta_o + \beta_1 X_{pH} + \beta_2 X_D + \beta_3 X_{Co} + \beta_4 X_T + \beta_{12} X_{pH} X_D + \beta_{13} X_{pH} X_{Co} + \beta_{14} X_{pH} X_T + \beta_{23} X_D X_{Co} + \beta_{24} X_D X_T + \beta_{34} X_{Co} X_T + \beta_{11} X_{pH}^2 + \beta_{22} X_D^2 + \beta_{33} X_{Co}^2 + \beta_{44} X_T^2 \quad \text{(Eq. 7)}$$

The quality of the polynomial equation (Eq. 7) was confirmed by the high correlation coefficients (R^2_{Adj} 0.997-0.991 and R^2_{Pred} 0.996-0.989), which are close to unity with high accuracy of approximation (R^2=0.998). A low significant error deviation in the conducted design further confirmed the suitability of the developed equation to fit the CV, MB, and MO adsorption responses. The RMSEP of 9.1, 14.04, and 11.83, RSEP of 18.63%, 25.36%, and 32.89% and calculated x^2 values of 7.68, 15.29 and 16.07 less than critical x^2 ($x^2_{\alpha,(n-1)}$41.34) were calculated for CV, MB, and MO adsorption responses, respectively. The statics low coefficient of variation (C.V. of 2.92%-3.72%) and adequate precision ratio of 82.65-97.99 greater than 4 [4], show an adequate signal for the polynomial equation (Eq. 7) to predict the dyes responses data. Moreover, the ANOVA results listed in Table (1) also indicated that the polynomial equation is significant. This is evident from the Student t-test (t_{model}=56.76-75.81>>t_{crit} 2.049) and Fisher's F-test (F_{model} = 447.33-626.28>>F_{crit} =$F_{0.05,df,(n-df+1)}$= 2.484) with a low probability value (p_{model} < 0.0001). Thus, the simulated model can be efficiently used in optimization of dyes adsorption.

3.2.2. Effects of model components on dyes adsorption efficiencies

The influence of the model components and their coefficient terms (β) on the studied dyes adsorption were tested by ANOVA tools listed in Table 1. StatisticalF_{Calc}, t_{Calc} and p-tools adopted that the linear model components showed high significant effects on dyes responses than their respective interactive and quadratic effects (Table 1). The results were reflected also by the estimated β values and the percent contribution (PC %) tabulated in Table 2. As seen, the linear components represented the highest influence level with a total PC% of 90.1%, 86.2%, and 85.2%; but, the quadratic components showed the lowest contribution with a total PC% of 4.2%, 4.6% and 4.8% for the CV, MB, and MO dyes adsorption, respectively. In general, the influential level of linear components can arrange as initial dyes concentrations (X_{Co}=44.8%, 46.2%, and 42.6%) > composite dose (X_D=35.4%, 36.97%, and 29.5%) > solution pH (X_{pH}=8.2%, 2.7%, and

12.6%) > temperature (X_T=1.7%, 0.36%, and 0.47%) on the dyes adsorption responses. Among the equation components, the interaction term of $X_D * X_T$ (PC%=0.001-0.05%; p=0.071-0.541) and quadratic temperature term (X_T^2, PC%=0.001-0.02%; p=0.236-0.984) showed the lowest influential effect on the dyes adsorption. As a fact, the coefficient sign determines the effect direction on the studied responses [4,13,20]. The estimated coefficient values (Table 2) showed that the X_D exhibited unfavorable or antagonistic effect (negative sign) on the dyes responses and pH variable (X_{pH}) on MO response. But the other variables showed positive coefficients terms (synergistic effect) along with X_{pH} on both CV and MB adsorption responses.

3.2.3. BBD-DOE optimization of adsorption process

The three-dimensional (3D) response surface contour plots are more helpful in facilitating the straightforward investigation of the experimental variables on the dyes responses [4,20]. Based on the simulated polynomial equation (Eq. 7), the 3D contour plots for the CV, MB and MO responses (q_e, µmol/g) are visualized in Fig (3). The 3D plots of $X_{pH} * X_D$ interactive term (Fig. 3a) showed that the P3C@CaO-HCN dose (X_D) exhibits an inverse influential effect on adsorption capacity, whereas the effect of solution pH is depends on the adsorbed dyes type. The q_e (µmol/g) of the basic CV and MB dyes increase with an increase in the entire pH range up to pH 7.5. While acidic MO dye adsorption capacity is higher at the median pH level of ≈ 6 and decreased at both very low and high pH levels. The pH-adsorption dependent suggested that the P3C@CaO-HCN adsorption mechanism is a complex interplay between electrostatic and non-electrostatic forces based on solution pH, pH_{ZPC} of the adsorbent and pka of dyes molecules (Scheme 1& cf. adsorption mechanism hereinafter). Because of hydrogen and hydroxyl ions are quite adsorbed on the surface sites and therefore the adsorption of dyes molecules is affected by the pH of the water. In addition, the solution pH affects the degree of adsorbent surface charge through protonation or deprotonation of functional groups on the adsorbent surface active sites and ionization of organic dyes pollutants.

The interactive effect of $X_{Co} * X_D$ on dyes adsorption (Fig. 3b) showed that the X_{Co} has a synergetic effect on the q_e (µmol/g) responses with decreasing the X_D level [4,20]. This trend is explained by assuming that the saturation of the all binding sites on the P3C@CaO-HCN surface is attained at the low X_D level of 0.5 g/l. However, with increase X_D level, a higher number of binding sites would generate that decrease the q_e (µmol/g) responses due to a vacant surface site that still unoccupied (equilibrium state not reached). The combined effect of $X_{Co} * X_T$ (Fig. 3c) showed that the temperature variable has a low synergetic influence on the dyes responses with parallel contour lines and no interaction withX_{Co}. This finding suggests that the experimental

temperature levels possess lower significant influence on dyes responses (q_e, μmol/g), which is confirmed by its lowest linear effect ratio of 91.59, 55.23 and 54.63 for CV, MB, and MO adsorption, respectively (Table 2).

In general, the results above revealed that the prepared P3C@CaO-HCN adsorbent has higher dyes adsorption capacities. Which is evident from an increase of q_e to 869.18, 1215.1, and 905.8 μmol/g for CV, MB, and MO, respectively at the adsorbent dose <0.75 g/l and increase X_{Co} up to 900 μmol/l. Consequently, the maximum operating conditions for the applied application were set by solving the developed polynomial regression model (Eq. 7) on the basis of BBD-DOE and the input variables levels with their linear, quadratic and interaction terms obtained. The predicted optimal variables levels at X_{Co}=1000 μmol/l were then computed as 5.9 pH, 0.5g/l P3C@CaO-HN sorbent, and 307 K solution temperature with desirability level of 0.96. At those optimum conditions, the maximum CV, MB, and MO predicted q_e(μmol/g) were 1013.9, 1418, and 1062.1, which are close to the experimental q_e(μmol/g) of 1018.2, 1429.5, and 1053.8, respectively.

3.3. Adsorption kinetics and thermodynamics

The effect of adsorption contact times on the dyes adsorption performance of P3C@CaO-HCN at temperature ranges from 288K to 328 K are shown in Fig (4). As seen, the dyes adsorption appear rapid rising at the first 4 h followed by gradual decrease up to equilibrium flattening rates starting at 6 h. Temperature also showed a low synergetic influence in the adsorbed amount ($q_{e,\exp,}$ entire set of Fig. 4a) with calculated t_{calc} value of 15.62-8.01, 7.18-5.38, and 8.21-5.62 and p-value range from 0.034 to 0.043 for CV, MB, and MO, respectively. To determine the adsorption mechanism, five kinetic models including pseudo-first-order model (PFOM), pseudo-second-order model (PSOM), Elovich, fractal like-pseudo first order (FL-PFOM), and mixed first and second-orders (MOE) kinetic models [21–24] were applied to simulate the dyes adsorption curvatures. Kinetic results and their corresponding mathematical model formula are listed in Table 3. According to the coefficients (R^2) and the resemblance between $q_{e,theo}$ and $q_{e,exp}$values in Table (3), the dye adsorption data can be interpreted by FL-PFOM and MOE kinetic expressions. A good fit mathematical equation does not depend only on theR^2, but it should be also accurate in predicting the experimental data. The good fitness to the FL-PFO and MOE mathematical models (Fig.4a) imply that the overall rate of dyes adsorption is time dependent on heterogenous sites on P3C@CaO-HCN surface that changing the adsorption behavior with the lapse of time [22,24].

The surface diffusion and intra-particle diffusion models such as the Boyd model and Weber and Morris (WMM) theory were further studied to determine the diffusion mechanism [23,25]. Application of WMM model (Fig. 4b) showed two-linearity adsorption stages. In the initial macro-pore diffusion phase I (R_1^2 0.902-0.991), most obtainable P3C@CaO-HCN adsorbing sites were utilized by 80- 90% of adsorbed dyes within $2.45h^{0.5} \approx 6$ h. The second micro-pore diffusion phase II (R_2^2 0.857-0.983) is attributed to a slow diffusion generated with the lapse of time. As seen in (Fig. 4b), the WMM empirical relationship stated that the intra-particle diffusion is not the rate-factor due to the two phases (I and II) lines do not pass through the origin. Diffusion rate constant of K_i (μmol g^{-1} $h^{0.5}$) were found to be exhibit a low significant dependent on the studied temperature ranges. Additionally, the Boyd model also showed that the calculated B_t points, the time coordinate of Boyd's expression, were scattered around the linear lines with good correlations values R^2 of 0.85-0.97 for dye adsorption (Fig. 4c). But, the linear lines of Boyd's curves (Fig. 4c) for the adsorbed dyes passing through the origin, which ascertained that the adsorption rates on P3C@CaO-HCN are governed by an initial boundary layer resistance and film diffusion mechanism.

The low significant effect of temperature levels (288 to 328 K) above was confirmed by the calculated thermodynamic constants using the Van't Hoff formula [21,26,27] at C_0=1000 μmol/l. The calculated positive enthalpy changes (ΔH°=8.58, 6.43, and 6.17 KJ/mol) and entropy changes (ΔS°=0.034, 0.034 and 0.027 KJ/mol) for CV, MB, and MO adsorbed dye show endothermic adsorption, which is consistent with the kinetics and BBD-DOE results. The low magnitude of calculated ΔH°, less than 20.9 kJ/mol, reveal that the adsorption is non-electrostatic physical type at optimum conditions [21,26]. In addition, the determined Gibb's free energy changes (ΔG°) for CV, MB, and MO dyes are ←1.26 to ←2.62 KJ/mol, ←3.46 to ←4.49 KJ/mol, and ←1.70 to ←2.51 KJ/mol at 288 K to 328 K, respectively. The negative values of ΔG° suggests spontaneity and feasibility of favorable adsorption by P3C@CaO-HCN. This kind of low significant temperature dependence of the adsorbed dyes by P3C@CaO-HCN adsorbent reflect the film diffusion mechanism of dye into the adsorbent.

3.4. Equilibrium isotherm studies

The isotherm provides information on how dyes adsorption and the commercial viability of the P3C@CaO-HCN materials for the adsorption application. A nonlinear regression solving of Langmuir, Tempkin, Freundlich, Redlich–Peterson, and Dubinin–Radushkevich isotherm models [21,26,27] were applied to simulate the equilibrium dyes adsorption results. The simulated nonlinear isotherm expressions for the adsorbed dyes by P3C@CaO-HCN and their coefficients

R^2 values are tabulated in Table 4. According to the determined coefficient R^2 value, R-P isotherm (R^2 > 0.99) showed best-fitting of dye adsorption data and poorest-fitting to D-R model (R^2 =0.92 -0.87). The R-P isotherm is a mix of Langmuir–Freundlich equations, and the R-P exponent constant (0< b < 1) can characterize the adsorption isotherm favorability [26]. Tabulated isotherm expressions (Table 4) and their graphical representations in Fig. 4d showed that the Langmuir is the preferable isotherm (R^2 0.99) for CV and MO adsorption (b=0.86 and 0.95); whereas MB adsorption obeys the Freundlich isotherm (R^2 0.99 and b=0.59). The dimensionless separation factor, R_L of 0.06-0.15 at C_o=1000 µmol/l, and Freundlich *n* exponent factor (*n*= 2.32-3.03) further confirmed favorable adsorption isotherm by P3C@CaO-HCN. Isotherm data shows that the P3C@CaO-HCN characterized by a certain degree of a heterogeneity binding sites (B_T=239.02-259.14 J/mol) as further revealed by Tempkin model ($R^2$0.94-0.98) [26,27]. Fig. (4d) also shows that the adsorption capacity of dye sharply increase to reach a plateau of maximum equilibrium trend at initial concentrations of 1200 µmol/l CV, 1450 µmol/l MB, and 1100 µmol/l MO dye. At these concentration points, the maximum experimental q_e (µmol/g) were recorded as 1227.8, 1915.8, and 1221 µmol/g for CV, MB, and MO dye, respectively.

3.5. Adsorption Mechanism

Regarding the resultant data above, it can suggested that the high performance of the P3C@Cao-HCN adsorbent toward both basic and acidic dyes (CV, MB and MO) adsorbates may be ascribed to a complex adsorption interactions. In addition, the adsorption interactions showed low B_T and ΔH° binding energy with a heterogeneity binding sites including electrostatic and non-electrostatic mechanisms, and its rate-controlling is a pH-dependent.

Herein, the potential mechanism involved was expected to be related to the electrostatic interaction as the predominant force at high and low pH levels. With increase pH > pH_{ZPC} (5.82), the CV and MB basic dyes adsorption were enhanced due to electrostatic forces developed between acidic surface sites of P3C@Cao-HCN and positive charge density of CV and MB cations, which unfavorable for the adsorption of MO acidic dye due to the electrostatic repulsion[4,28–30]. In this case, it can be said that the adsorption of cationic dyes is fine and can more easily take place when usage of alkaline pH. At high acidic condition (pH< 4), the adsorption capacities of basic (CV and MB) and acidic (MO) dyes decreased, because of the higher number of protonation H^+ levels. The high concentrations of positive H^+ ions associate to the P3C@CaO-HCN surface and form positively protonated surface sites. The developed protonated surface generate electrostatic repulsion with basic CV and MB cations and hydronium counter ions around acidic MO anions (SO_3^-) in the bulk water solution, leading to decrease their

adsorption capacity. Similar observation was recorded at a high alkaline pH (pH >8) because of a relatively higher number of $HO^{\leftarrow}$ groups in solution. In fact, such electrostatic interaction mechanism is possible between the electron pairs of N-H group in the 1H-pyrrole derivative of the P3C functionalities or tri-s-triazine units (bridging C–NH–C units) of HCN. Otherwise, at near neutral pH≈ 6 approximately equal pH_{ZPC} (5.82) > pKa of CV (pKa=5.31), MB (pKa=3.8) and MO (pKa=3.47), the main predominant mechanism could be controlled by non-electrostatic attraction forces. Such non-electrostatic interactions could including π- π stacking interaction and hydrophobic-hydrophobic mechanisms, which could be more favored for MO anionic dye. At which, the π- π adsorption mechanism can developed between the π-orbitals in the aromatic ring of dye molecules and delocalized π-electrons of the C=C double bonds of HCN nanosheets or aromatic binding sites on the P3C functional surface of adsorbents. P3C@CaO-HCN can also interact with dye molecules via hydrophobic-hydrophobic mechanism between the di-phenyl groups in the pyrrolone derivatives of P3C functionality at positions 4 and 5 of 1H-pyrrole derivative and aromatic rings of dye molecules. This is worthwhile to point out that the P3C@Cao-HCN is effective adsorbent in the adsorption removal of both cationic and anionic organic dyes with counter charges.

3.6. Models validation and error analysis

Statistical error parameters for the best-fitted models were computed in this work to confirm the suitability of the overall simulated kinetic (FL-PFO and MOE) and isotherm (Langmuir, Freundlich, and R-P) mathematical expressions to the experimental results. First, a non-parametric Mann–Whitney U-test, a parametric (unpaired) t-test and one-way ANOVA were conducted to test significance difference between the experimental (Y_{exp}) and the predicted (Y_{pred}) dyes adsorption capacities [4]. The calculated Mann–Whitney z-score of 0.75-0.04, less than unity, associated with the two-tailed p-value of 0.59-0.987 greater than the chosen level of p=0.05 (95% confidence) imply the suitability of the above selected fitted expressions. Also, the calculated statistic tools from one-way ANOVA were found to be in the range of t_{cal}=0.001-0.39 and F_{cal}=0.0001-0.31, which are lower than the critical values of t_{crit}=±2.41, and F_{crit}= 3.73. Second, the experimental and predicted output response variables (q_e, µmol/g) for each set of validation points were used to compute the Chi-square (x^2), RSEP, RMSEP, and %ARE error values. Notably, a low error results were recorded using RMSEP (2.08 -2.81), RSEP (1.12- 2.13), % ARE (2.17%-4.65%), and x^2 (0.13-0.15<< critical $x^2_{\alpha,(df=n-1)}$ of 16.92) with a high correlation (R^2 = 0.992 to 0.999) between Y_{exp} and Y_{pred}. In this case, at 95% certainty, the experimental dyes adsorption results by P3C@CaoO-HCN were well described by the fitted

mathematical expressions above under the calculated statics with the lowest error and the significant difference between the two set of output responses (Y_{pred} and Y_{exp}) [4].

3.7. Antimicrobial activity

The synthesized P3C@CaO-HCN nanocomposite was further screened for its in vitro antimicrobial activity against three free-living pathogenic strains of *Escherichia coli* and *Pseudomonas aeruginosa* bacterial and *Candida albicans* yeast. Luria-Bertani (LB) broth containing different concentrations of P3C@CaO-HCN (C_o= 100, 250, 500, 1000, and 2500 mg/l) and 10^5 CFU/ml initial pathogenic cell was used to test the antimicrobial activity at 310 K and 150 rpm shaking speed. An inhibitory percentage rate (I%, Eq. 9) at the mid-exponential microbial growth was measured against microbial culture blank as a positive control.

$$I\% = \frac{(CFU_{PC} - CFU_{ACo})}{CFU_{PC}} x100 \text{ (Eq. 9)}$$

Where, CFU_{PC} and CFU_{ACo} are the total strains colony forming unit (CFU/ml) in the absence and presence of composite, respectively. The inhibitory rate (I%) of P3C@CaO-HCN against *E. coli*, *P. aeruginosa* and *C. albicans* pathogens is shown in Fig (5). It is seen that the cytotoxicity effect toward the three pathogens was increased with the increasing concentration of P3C@CaO-HCN. The visualized reduced of cell viability was escalated with *E. coli* compared to *P. aeruginosa* and *C. albicans* at given concentrations, which implied that the antimicrobial activity of P3C@CaO-HCN was not only P3C@CaO-HCN dependent but also microbial dependent. As shown in Fig (5), the P3C@CaO-HCN loaded cultures also exhibited a high significant antimicrobial activity with reduction percentage on E. *coli* (93.5%) and C. *albicans* (85.8%) compared to a moderate I% against *P. aeruginosa* (61.54%) at C_o of 2500 mg/l P3C@CaO-HCN. Also, the P3C@CaO-HCN showed minimum inhibitory concentration (MIC) at 500 mg/l with I% of 87.9%, 46.9%, and 72.5% for *E. coli*, *P. aeruginosa*, and *C. albicans*, respectively. Lossing microbial viability may result from the free cyanide (C≡N) group on 4, 5-diphenyl-2-thioxo-2, 5-dihydro-1H-pyrrole-3-cabonitrile functionality and protonated g-C_3N_4 (HCN) sheet. The composite provide electrostatic adsorption of a negatively charged microbial surface onto positive HCN sheet, and subsequently, the free C≡N functionalities tightly bound to ubiquinone whole cells (Scheme 1). This may lead to induce microbial membrane stress and hence disrupting their metabolic system that leading to cell death [10,11].

4. Conclusions

In this work, P3C@Cao-HCN nanocomposite, a new multi-functional nanomaterial, was fabricated for wastewater remediation from organic dye and microbial contaminants. The

P3C@Cao-HCN was prepared by the reaction of 4, 5-diphenyl-2-thioxo-2, 5-dihydro-1H-pyrrole-3-cabonitrile with CaO nanoparticles impregnated onto protonated carbon nitride (HCN). Adsorption experiment of CV, MB, and MO organic dye using Box-Behnken design outlined that the adsorption mechanism of P3C@Cao-HCN depends on the molecular dye structure and the adsorbate surface aspect, which varies with solution pH level. The adsorption data was fitted with both the fractal like-pseudo first-order (FL-PFOM), and mixed first and second-orders (MOE) kinetic models and Redlich–Peterson (R-P) isotherm well. The validation data confirmed the high suitability of the selected models to simulate the adsorption data (R^2>0.99, RMSEP ≤ 2.81, RSEP ≤2.13, % ARE ≤ 4.65%, and $x^2 \leq 0.15$ less than critical $x^2_{\alpha,(df=n-1)}$ of 16.92) at the probability level of 0.05. P3C@CaO-HCN proved to be a suitable novel antimicrobial nanomaterial against *E. coli* and *P. aeruginosa* and *C. albicans* pathogens in this work for the first time. The inhibition rates (I%) of 87.9%, 46.9%, and 72.5% were attained at MIC of 500 mg/l P3C@CaO-HCN for *E. coli*, *P. aeruginosa*, and *C. albicans*, respectively due to damaging of microbial membrane by the free cyanide (C≡N) functionality and protonated g-C_3N_4 (HCN) sheet. The notable high dye adsorption capacity and antimicrobial activity by P3C@CaO-HCN offers its promising applications for industrial wastewater remediation and management.

5. References

1 V. S. Mane and P. V. V. Babu, *J. Taiwan Inst. Chem. Eng.*, 2013, **44**, 81–88.

2 C. Djilani, R. Zaghdoudi, F. Djazi, B. Bouchekima, A. Lallam, A. Modarressi and M. Rogalski, *J. Taiwan Inst. Chem. Eng.*, 2015, **53**, 112–121.

3 A. Duta and M. Visa, *J. Photochem. Photobiol. A Chem.*, 2015, **306**, 21–30.

4 K. P. Singh, S. Gupta, A. K. Singh and S. Sinha, *J. Hazard. Mater.*, 2011, **186**, 1462–1473.

5 M. Roosta, M. Ghaedi, A. Daneshfar, R. Sahraei and A. Asghari, *Ultrason. Sonochem.*, 2014, **21**, 242–252.

6 E. Haque, J. W. Jun and S. H. Jhung, *J. Hazard. Mater.*, 2011, **185**, 507–511.

7 S. Li, *Bioresour. Technol.*, 2010, **101**, 2197–2202.

8 G. Z. Kyzas, A. Koltsakidou, S. G. Nanaki, D. N. Bikiaris and D. A. Lambropoulou, *Sci. Total Environ.*, 2015, **537**, 411–420.

9 J.-G. Yu, X.-H. Zhao, H. Yang, X.-H. Chen, Q. Yang, L.-Y. Yu, J.-H. Jiang and X.-Q. Chen, *Sci. Total Environ.*, 2014, **482**, 241–251.

10 Y. Jiang, J.-L. Gong, G.-M. Zeng, X.-M. Ou, Y.-N. Chang, C.-H. Deng, J. Zhang, H.-Y. Liu and S.-Y. Huang, *Int. J. Biol. Macromol.*, 2016, **82**, 702–710.

11 F. A. Al-Sagheer, E. I. Ibrahim and K. D. Khalil, *Eur. Polym. J.*, 2014, **58**, 164–172.

12 A. I. Hashem, W. S. I. Abou-Elmagd and A. Abd-Elaziz, *Eur. Chem. Bull.*, 2014, **3**, 1064–1068.
13 A. A. Oladipo, M. Gazi and E. Yilmaz, *Chem. Eng. Res. Des.*, 2015, **104**, 264–279.
14 R. Slimani, I. El Ouahabi, F. Abidi, M. El Haddad, A. Regti, M. R. Laamari, S. El Antri and S. Lazar, *J. Taiwan Inst. Chem. Eng.*, 2014, **45**, 1578–1587.
15 L. Pi, R. Jiang, W. Zhou, H. Zhu, W. Xiao, D. Wang and X. Mao, *Appl. Surf. Sci.*, 2015, **358**, 231–239.
16 G. Liu, X. Yang, T. Li, Y. She, S. Wang, J. Wang, M. Zhang, F. Jin, M. Jin and H. Shao, *Mater. Lett.*, 2015, **160**, 472–475.
17 W. Liu, M. Wang, C. Xu and S. Chen, *Chem. Eng. J.*, 2012, **209**, 386–393.
18 W.-J. Ong, L.-L. Tan, S.-P. Chai, S.-T. Yong and A. R. Mohamed, *Nano Energy*, 2015, **13**, 757–770.
19 J. Lützenkirchen, T. Preočanin, D. Kovačević, V. Tomišić, L. Lövgren and N. Kallay, *Croat. Chem. Acta*, 2012, **85**, 391–417.
20 P. Tripathi, V. C. Srivastava and A. Kumar, *Desalination*, 2009, **249**, 1273–1279.
21 S. A. Younis, N. S. El-Gendy, W. I. El-Azab, Y. M. Moustafa and A. I. Hashem, *Energy Sources, Part A Recover. Util. Environ. Eff.*, 2014, **36**, 2566–2578.
22 M. Haerifar and S. Azizian, *J. Phys. Chem. C*, 2014, **118**, 1129–1134.
23 A. W. Marczewski, *Appl. Surf. Sci.*, 2010, **256**, 5145–5152.
24 N. Bakhtiari and S. Azizian, *J. Mol. Liq.*, 2015, **206**, 114–118.
25 P. S. Kumar, S. Ramalingam, C. Senthamarai, M. Niranjanaa, P. Vijayalakshmi and S. Sivanesan, *Desalination*, 2010, **261**, 52–60.
26 B. Tanhaei, A. Ayati, M. Lahtinen and M. Sillanpää, *Chem. Eng. J.*, 2015, **259**, 1–10.
27 M. Arshadi, F. S. Vahid, J. W. L. Salvacion and M. Soleymanzadeh, *Appl. Surf. Sci.*, 2013, **280**, 726–736.
28 J. R. Kim, B. Santiano, H. Kim and E. Kan, 2013.
29 M. Doğan, Y. Özdemir and M. Alkan, *Dye. Pigment.*, 2007, **75**, 701–713.
30 V. Vimonses, B. Jin and C. W. K. Chow, *J. Hazard. Mater.*, 2010, **177**, 420–427.

526
527

528 **Figure Captions**

529 Fig. 1: a) XRD patterns (CaO NPs, HCN, and CaO-HCN) and (b) FT-IR spectra of (i) P3C, (ii)
530 CaO NPs, (ii) HCN, (iv) CaO-HCN, and (v) P3C@CaO-HCN.

531 Fig. 2: a) TEM image of P3C@CaO-HCN composite, and b) The pH_{ZPC} determination by
532 potentiometric and salt addition methods.

533 Fig. 3: 3D response surface contour plots of CV, MB, and MO dyes adsorption capacities versus
534 interaction of: (a) pH and adsorbent dose ($X_{pH}X_D$), (b) initial dyes concentrations and adsorbent
535 dose ($X_{Co}X_D$), and (c) initial dyes concentrations and temperature ($X_{Co}X_T$).

536 Fig. 4: (a) Effect of contact time on P3C@CaO-HCN adsorption capacities (b) Intra-particle
537 diffusion model; (c) Boyed surface diffusion model; and (d) isotherm models of CV, MB, and
538 MO adsorptions.

539 Fig. 5: Antimicrobial activity of P3C@CaO-HCN against *E. coli*, *P. aeruginosa* and *C. albicans*
540 microbial pathogen

541

542

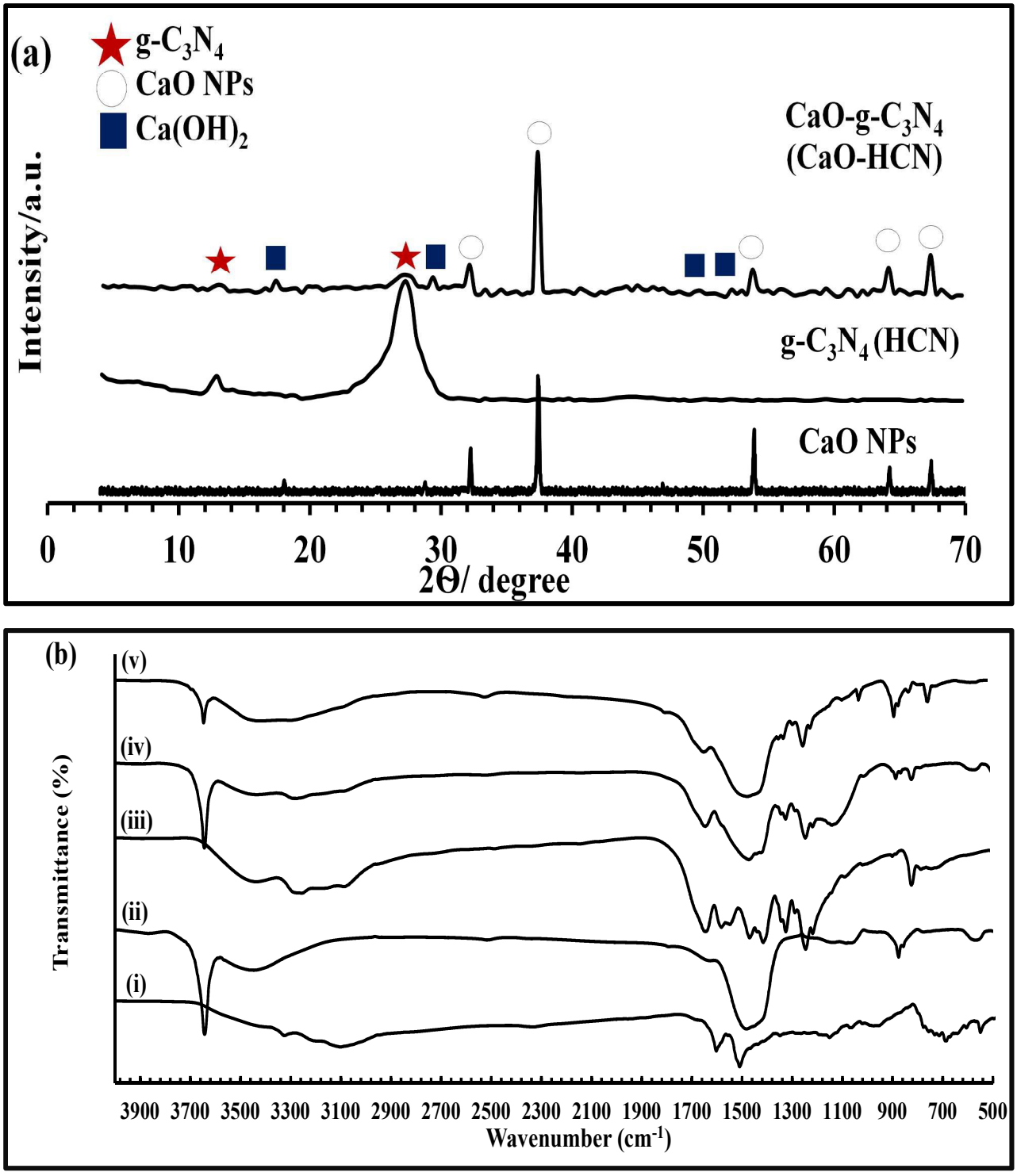

Fig. 1: a) XRD patterns (CaO NPs, HCN, and CaO-HCN) and (b) FT-IR spectra of (i) P3C, (ii) CaO NPs, (ii) HCN, (iv) CaO-HCN, and (v) P3C@CaO-HCN.

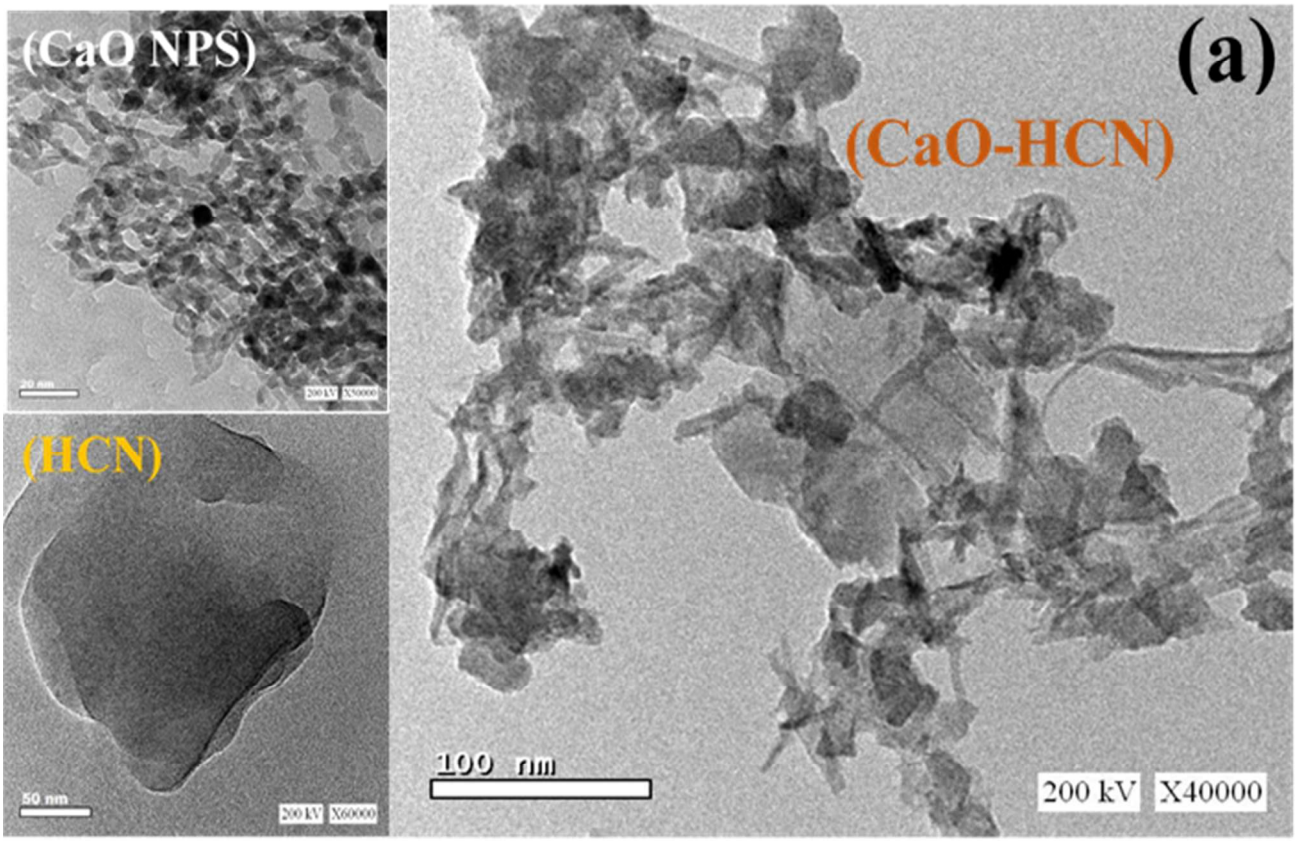

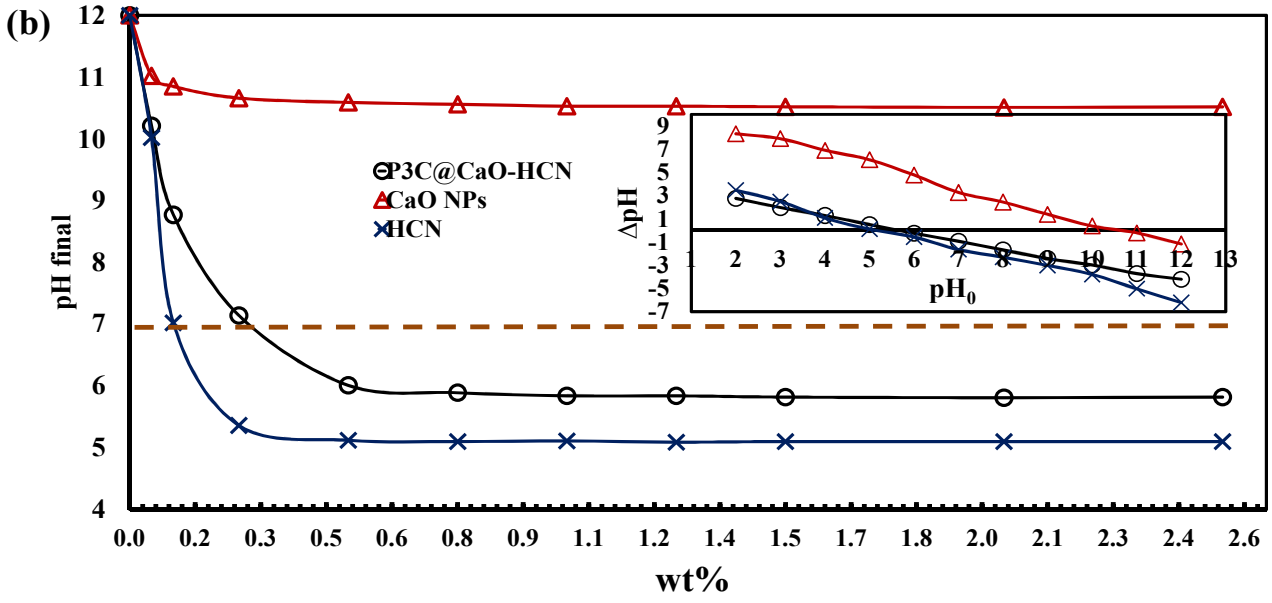

Fig. 2: a) TEM image of P3C@CaO-HCN composite, and b) The pH_{ZPC} determination by potentiometric and salt addition methods.

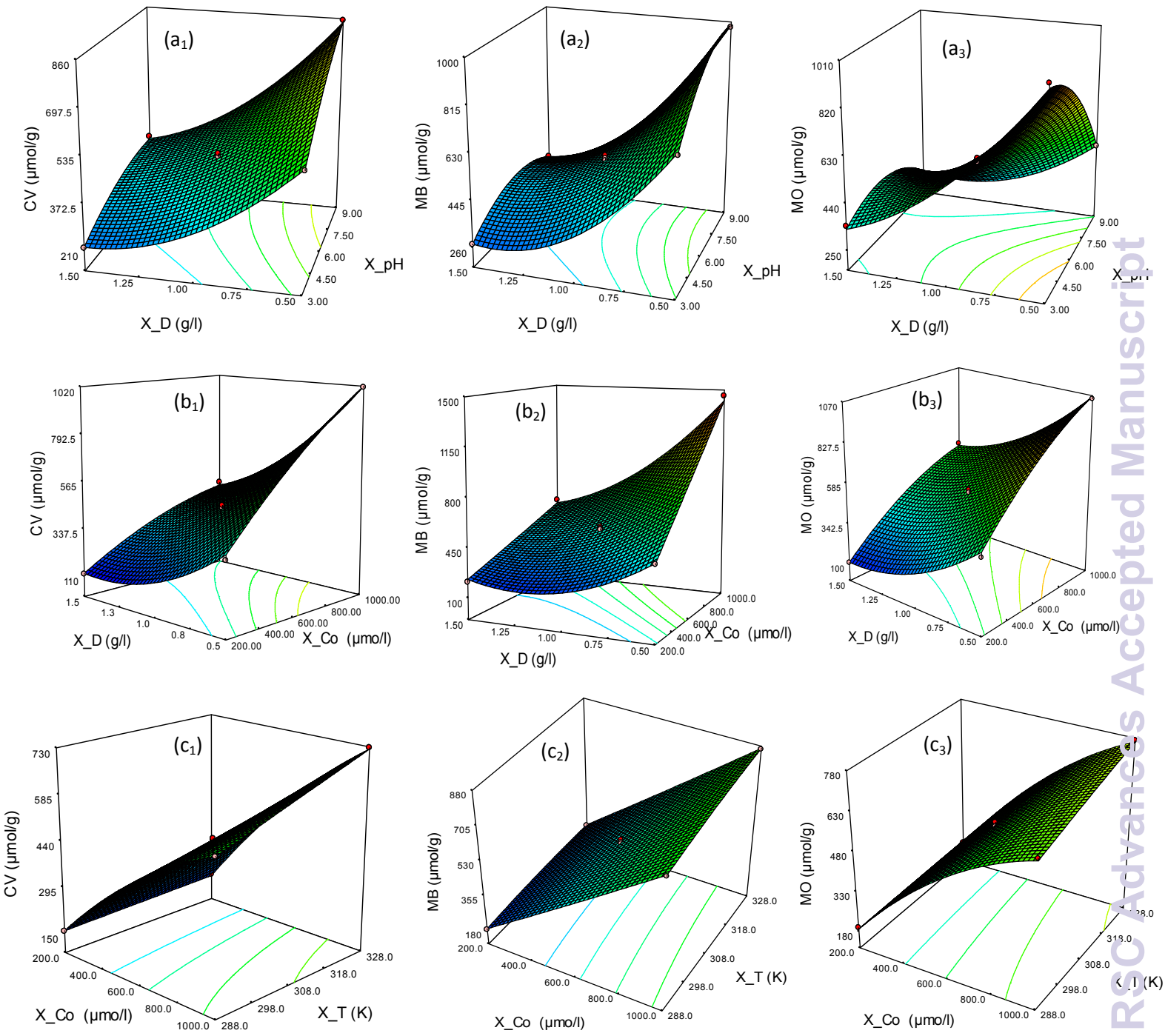

Fig. 3: 3D response surface contour plots of CV, MB, and MO dyes adsorption capacities versus interaction of: (a) pH and adsorbent dose ($X_{pH}X_D$), (b) initial dyes concentrations and adsorbent dose ($X_{Co}X_D$), and (c) initial dyes concentrations and temperature ($X_{Co}X_T$).

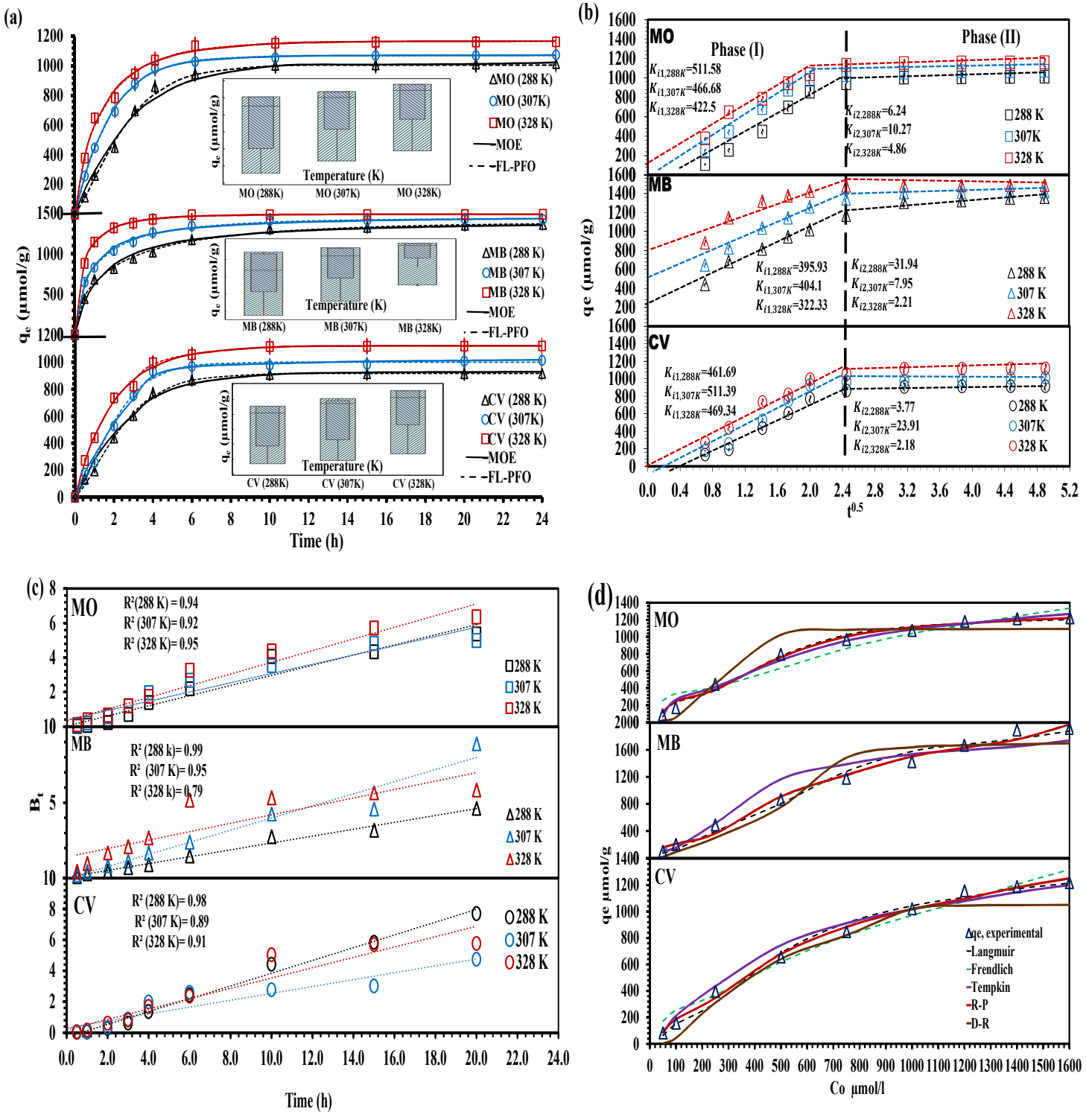

Fig. 4: (a) Effect of contact time on P3C@CaO-HCN adsorption capacities (b) Intra-particle diffusion model; (c) Boyed surface diffusion model; and (d) isotherm models of CV, MB, and MO adsorptions.

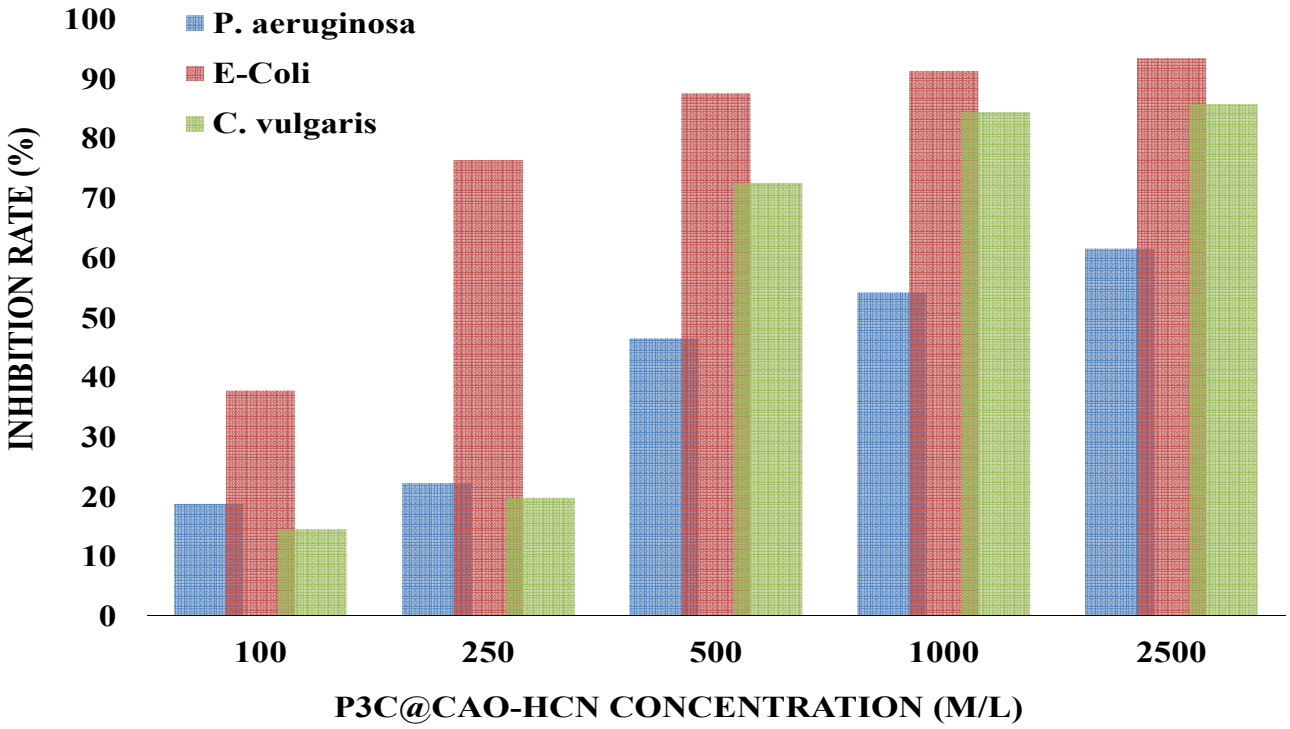

Fig. 5: Antimicrobial activity of P3C@CaO-HCN against *E. coli*, *P. aeruginosa* and *C. albicans* microbial pathogen.

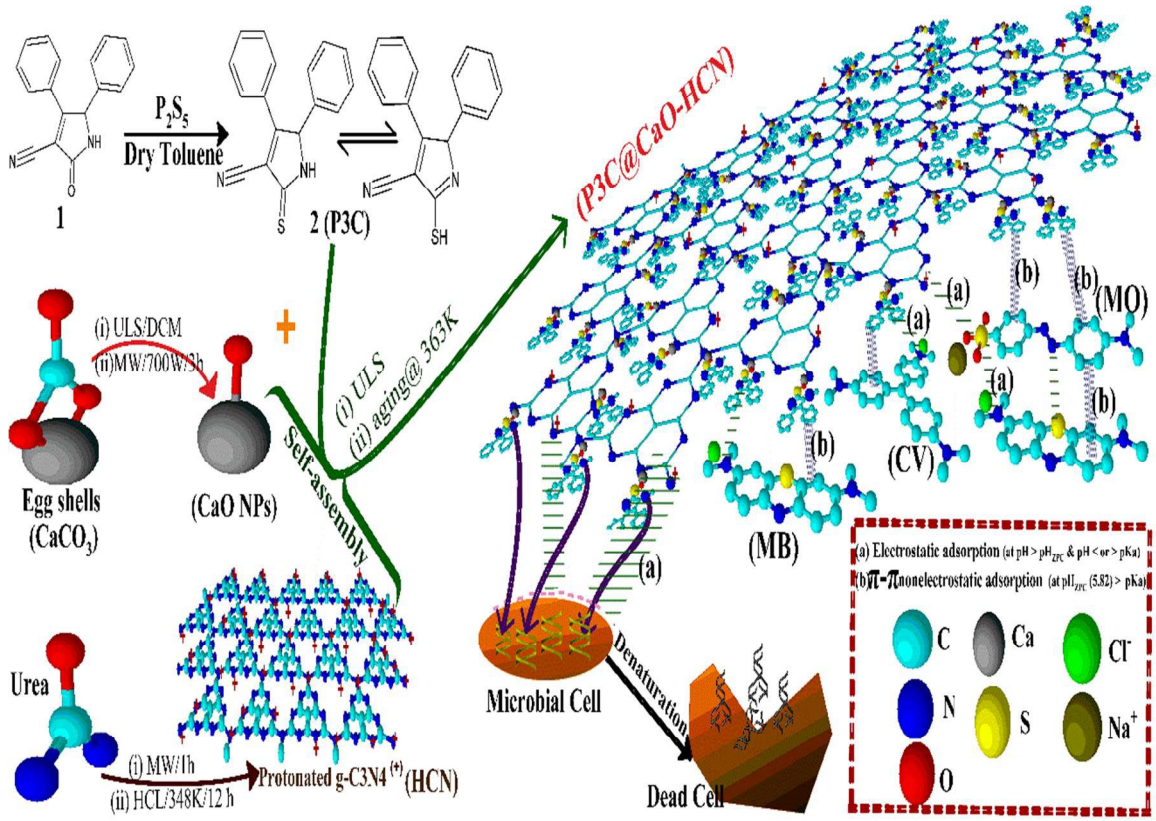

Scheme 1: diagram of P3C@CaO-HCN nanocomposite preparation procedure, and proposed adsorption and antimicrobial mechanisms.

Table 1: ANOVA[1] results of the CV, MB, and MO responses by P3C@CaO-HCN.

Source	df	SS			F-value			Prob>F		
		CV	MB	MO	CV	MB	MO	CV	MB	MO
Model	**14**	1504132.8	2553355.5	1912533.8	626.3	532.5	467.0	< 0.0001	< 0.0001	< 0.0001
X_{pH}	**1**	123848.6	68927.1	242111.8	721.9	201.3	827.7	< 0.0001	< 0.0001	< 0.0001
X_D	**1**	533950.1	945749.9	565372.2	3112.5	2761.5	1932.8	< 0.0001	< 0.0001	< 0.0001
X_{Co}	**1**	674328.3	1180919.0	816988.7	3930.8	3448.1	2793.1	< 0.0001	< 0.0001	< 0.0001
X_T	**1**	25167.8	9150.5	8954.0	146.7	26.7	30.6	< 0.0001	0.0001	< 0.0001
$X_{pH}X_D$	**1**	6048.7	9096.6	45405.4	35.3	26.6	155.2	< 0.0001	0.0001	< 0.0001
$X_{pH}X_{Co}$	**1**	18413.6	9108.9	37073.9	107.3	26.6	126.7	< 0.0001	0.0001	< 0.0001
$X_{pH}X_T$	**1**	4175.6	1253.0	221.5	24.3	3.7	0.8	0.0002	0.0765	0.3741
X_DX_{Co}	**1**	28218.4	97195.0	4961.1	164.5	283.8	17.0	< 0.0001	< 0.0001	0.0007
X_DX_T	**1**	67.3	522.5	999.7	0.4	1.5	3.4	0.5413	0.2371	0.0714
$X_{Co}X_T$	**1**	6300.1	892.8	3100.0	36.7	2.6	10.6	< 0.0001	0.1287	0.0040
X_{pH}^2	**1**	7428.3	46226.8	62815.4	43.3	135.0	213.0	< 0.0001	< 0.0001	< 0.0001
X_D^2	**1**	48461.4	142760.8	62708.5	282.5	416.8	216.1	< 0.0001	< 0.0001	< 0.0001
X_{Co}^2	**1**	11976.8	75.5	30338.0	69.8	0.2	102.5	< 0.0001	0.6459	< 0.0001
X_T^2	**1**	0.1	526.1	69.4	0.04	1.5	0.2	0.9841	0.2356	0.6154
Residual	**14**	2401.7	4794.7	3679.3						
Lack of Fit	**10**	2281.9	4493.7	3449.2	7.6	6.0	2.1	0.0326	0.0499	0.0496
Pure Error	**4**	119.8	301.0	230.2						
Cor Total	**28**	1506534.5	2558150.2	1916213.2						

Table 2: Multiple regression[2] and BBD-DOE coefficients results.

[1] ANOVA: analysis of variance determined by Design-Expert (v. 7.0.1) software.

Model components	Model terms	Effect			Estimated coefficient			t-value			PC[3] (%)		
		CV	MB	MO	CV	MB	MO	CV	MB	MO	CV	MB	MO
Intercept	β_o	----	----	----	444.1	519.4	522.1	75.81	62.76	72.01	----	----	----
X_{pH}	β_1	203.18	151.58	-284.08	101.6	75.8	-142.0	26.87	14.19	-30.35	8.22	2.69	12.63
X_D	β_2	-421.88	-561.47	-434.12	-210.9	-280.7	-217.1	-55.79	-52.55	-46.38	35.44	36.97	29.50
X_{Co}	β_3	474.11	627.41	521.85	237.1	313.7	260.9	62.7	58.72	55.76	44.76	46.16	42.64
X_T	β_4	91.59	55.23	54.63	45.8	27.6	27.3	12.11	5.17	5.84	1.67	0.36	0.47
$X_{pH}X_D$	β_{12}	-77.77	-95.38	213.09	-38.9	-47.7	106.5	-5.94	-5.15	13.14	0.40	0.36	2.37
$X_{pH}X_{Co}$	β_{13}	135.7	95.44	-192.55	67.8	47.7	-96.3	10.36	5.16	-11.88	1.22	0.36	1.93
$X_{pH}X_T$	β_{14}	64.62	35.4	-14.88	32.3	17.7	-7.4	4.93	1.91	-0.92	0.28	0.05	0.01
X_DX_{Co}	β_{23}	-167.98	-311.76	-70.44	-84.0	-155.9	-35.2	-12.83	-16.85	-4.34	1.87	3.80	0.26
X_DX_T	β_{24}	-8.2	-22.86	-31.62	-4.1	-11.4	-15.8	-0.63	-1.24	-1.95	0.001	0.02	0.05
$X_{Co}X_T$	β_{34}	79.37	29.88	55.68	39.7	14.9	27.8	6.06	1.61	3.43	0.42	0.03	0.16
X_{pH}^2	β_{11}	-67.68	-168.84	-196.82	-33.8	-84.4	-98.4	-6.58	-11.62	-15.46	0.74	2.98	3.82
X_D^2	β_{22}	172.87	296.71	196.65	86.4	148.4	98.3	16.81	20.42	15.45	3.99	6.01	4.34
X_{Co}^2	β_{33}	-85.94	6.82	-136.78	-43.0	3.4	-68.4	-8.36	0.47	-10.74	0.82	0.01	1.61
X_T^2	β_{44}	-0.21	-18.01	-6.54	-0.1	-9.0	-3.3	-0.02	-1.24	-0.51	0.001	0.02	0.001

[2] Multiple regression analysis calculated by MINITAB (v. 17) software.

[3] The percent contribution (PC %) = $SS/\sum SS \times 100$.

Table 3: Kinetics constants for the adsorption of CV, MB, and MO by P3C@CaO-HCN at different temperatures (288 K, 307 K, and 328 K).

Kinetic parameters		CV			MB			MO			Kinetic equations
		288 K	307 K	328 K	288 K	307 K	328 K	288 K	307 K	328 K	
Experimental q_e (µmol. g^{-1})		915.40	1014.00	1120.32	1360.07	1421.99	1487.54	1014.01	1073.90	1161.79	
PFOM	q_o (µmol. g^{-1})	933.72	1017.57	1118.02	1298.28	1368.71	1452.65	1024.15	1070.77	1145.34	$q_t = q_o(1 - \exp(\leftarrow K_1 t))$
	K_1 (h^{-1})	0.35	0.42	0.51	0.52	0.87	1.66	0.35	0.55	0.68	
	R^2	0.98	0.97	0.99	0.91	0.91	0.94	0.98	0.99	0.97	
FL-PFO	q_o (µmol. g^{-1})	916.1	1009.69	1121.61	1365.52	1436.59	1486.35	1010.34	1068.95	1166.77	$q_t = q_o(1 - \exp(\leftarrow K_1 t^{\alpha}))$
	K_1 (h^{-1})	0.26	0.32	0.52	0.61	0.87	1.41	0.28	0.54	0.72	
	α	1.34	1.37	0.96	0.59	0.59	0.62	1.27	1.04	0.79	
	R^2	0.996	0.99	0.995	0.993	0.996	0.997	0.992	0.998	0.991	
PSOM	q_o (µmol. g^{-1})	1080.16	1157.38	1243.37	1409.54	1470.08	1512.28	1186.13	1187.42	1249.21	$q_t = K_2 q_o^2 t \Big/ 1 + K_2 q_o t$
	K_2 (g. .µmol^{-1}. h^{-1})	0.0004	0.0004	0.0005	0.001	0.001	0.002	0.0003	0.0006	0.001	
	$t^{1/2}$ (h)	2.46	1.96	1.46	0.70	0.68	0.33	2.48	1.34	1.00	
	R^2	0.94	0.93	0.97	0.98	0.98	0.99	0.95	0.96	0.98	
Elovich	β (µmol. g^{-1}. h^{-1})	226.39	232.11	225.72	242.61	204.65	137.59	250.01	211.05	196.67	$q_t = \beta \ln(\propto \beta t)$
	∝ (g.µmol^{-1}. h^{-2})	0.02	0.02	0.05	0.07	0.35	29.77	0.02	0.06	0.14	
	R^2	0.90	0.86	0.90	0.94	0.92	0.80	0.92	0.87	0.88	
MOE	q_o (µmol. g^{-1})	913.94	1016.59	1121.24	1389.87	1433.29	1488.42	1021.18	1071.78	1167.17	$q_t = q_o \frac{1 - \exp(\leftarrow K_1 t)}{1 - F \exp(\leftarrow K_1 t)}$
	K_1 (h^{-1})	0.35	0.42	0.45	0.01	0.03	0.36	0.35	0.55	0.33	
	F	0.001	0.001	0.154	1.000	0.975	0.866	0.001	0.001	0.640	
	R^2	0.981	0.973	0.995	0.982	0.988	0.998	0.982	0.998	0.990	

Table 4: Isothermal equations and determination coefficients of CV, MB, and MO dye adsorption onto P3C@CaO-HCN adsorbent.

Isotherm models	Simulated mathematical isotherm equations			R^2		
	CV	MB	MO	CV	MB	MO
Langmuir	$q_e = 1449.40\frac{0.005C_e}{1+0.005C_e}$ R_L=0.154	$q_e = 2221.56\frac{0.008C_e}{1+0.008C_e}$ R_L=0.11	$q_e = 1284.37\frac{0.015C_e}{1+0.015C_e}$ R_L=0.06	0.99	0.95	0.99
Freundlich	$q_e = 67.192C_e^{1/2.32}$	$q_e = 203.26C_e^{1/2.84}$	$q_e = 137.33C_e^{1/3.03}$	0.97	0.99	0.94
Tempkin	$q_e = 259.14\ln(0.103C_e)$	$q_e = 253.69\ln(0.147C_e)$	$q_e = 239.02\ln(0.2C_e)$	0.98	0.94	0.98
Redlich–Peterson (R-P)	$q_e = \frac{11.399C_e}{1+0.027C_e^{0.86}}$	$q_e = \frac{1395.09C_e}{1+6.38C_e^{0.59}}$	$q_e = \frac{21.28C_e}{1+0.02C_e^{0.95}}$	0.99	0.99	0.99
Dubinin–Radushkevich (D-R)	$q_e = 1053.88\exp(-0.001\varepsilon^2)$	$q_e = 1713.38\exp(-0.0006\varepsilon^2)$	$q_e = 1092.61\exp(-0.0001\varepsilon^2)$	0.87	0.87	0.92